Eur. Phys. J. E (2017) **40**: 7
DOI 10.1140/epje/i2017-11493-8

THE EUROPEAN PHYSICAL JOURNAL E

Regular Article

Phase behaviour in complementary DNA-coated gold nanoparticles and fd-viruses mixtures: a numerical study*

Massimiliano Chiappini[1,a], Erika Eiser[2,b], and Francesco Sciortino[1,c]

[1] Physics Department, University of Rome "La Sapienza", Rome, Italy
[2] University of Cambridge, Cavendish Laboratory, J. J. Thomson Avenue, Cambridge CB3 0HE, UK

Received 13 September 2016 and Received in final form 16 December 2016
Published online: 24 January 2017 –

Abstract. A new gel-forming colloidal system based on a binary mixture of fd-viruses and gold nanoparticles functionalized with complementary DNA single strands has been recently introduced. Upon quenching below the DNA melt temperature, such a system results in a highly porous gel state, that may be developed in a new functional material of tunable porosity. In order to shed light on the gelation mechanism, we introduce a model closely mimicking the experimental one and we explore via Monte Carlo simulations its equilibrium phase diagram. Specifically, we model the system as a binary mixture of hard rods and hard spheres mutually interacting via a short-range square-well attractive potential. In the experimental conditions, we find evidence of a phase separation occurring either via nucleation-and-growth or via spinodal decomposition. The spinodal decomposition leads to the formation of small clusters of bonded rods and spheres whose further diffusion and aggregation leads to the formation of a percolating network in the system. Our results are consistent with the hypothesis that the mixture of DNA-coated fd-viruses and gold nanoparticles undergoes a non-equilibrium gelation via an arrested spinodal decomposition mechanism.

1 Introduction

Since Onsager's theoretical prediction of the isotropic-to-nematic transition of hard rods [1], filamentous Tobacco Mosaic viruses [2–4] and bacteriophage fd-viruses [5, 6] have been used among others (*e.g.*, boehmite [7], akaganeite [8], silica [9], sepiolite clay [10], protein fibrils [11], etc.) as rod-like colloids to test Onsager's predictions of the phase behavior of anisotropic particles. Indeed, viruses are particularly appealing as an experimental realization of rod-like colloidal particles both because of their high monodispersity and because of their effective aspect ratio that can be tuned from 10 up to 100 continuously. Such a variable aspect ratio is possible —given the charge of the side-coat proteins— by playing with the ionic strength in solution and thus tuning the effective range of repulsion between the viruses. A comprehensive review can be found in ref. [5]. More recently the phase diagram of hard rods solutions has been extended to account for the presence of non-adsorbing polymers or hard spheres causing a well-defined short-ranged depletion attraction [6, 11–13]. Such binary systems containing asymmetric particles lead to many new phases.

An even more controlled attraction between different types of colloids can be achieved by functionalizing them with short single-stranded (ss)DNA [14–16]. It is possible to make use of the high specificity of DNA in terms of the sequence of bases (Adenine, Cytosine, Thymine and Guanine) along the ssDNA backbone, allowing it to reversibly bind only to its complementary sequence purely via hydrogen bonds. In this way colloids grafted with a single strand of DNA called α can only bind to colloids holding the complementary sequence α' when cooled below the melt temperature T_m of the specific DNA sequence. T_m is defined as the temperature where half of all possible base-pairs between complementary strands are formed. Hence, below T_m DNA-driven aggregation settles in, and colloids functionalized with complementary DNA single strands start to aggregate. Recently, ssDNA have been covalently bound to the side-coat proteins of fd-virions [17]. In particular, one of us [18] experimentally studied the aggregation behaviour of a binary system of fd-virions and gold nanoparticles (gold-NPs) for varying number ratios but

* Supplementary material in the form of two .mp4 files and one .pdf file available from the Journal web page at http://dx.doi.org/10.1140/epje/i2017-11493-8

[a] e-mail: massimilianochiappini@gmail.com
[b] e-mail: ee247@cam.ac.uk
[c] e-mail: francesco.sciortino@uniroma1.it

overall low colloidal volume fractions. The binding rules were chosen such that the roughly 880 nm long, α DNA-coated virions could only bind to 50 nm large gold colloids, densely grafted with α' DNA [18]. A binary mixture of semi-flexible rods (the fd-viruses) and spheres (the gold nanoparticles) mutually interacting via a short-range thermally reversible binding attraction was therefore obtained. When the initially homogeneously mixed rod-sphere system was quenched from the fluid phase into the two-phase region below T_m rapid aggregation occurred [18], possibly driven by spinodal decomposition at the initial stages. At a second stage, the incipient spinodal demixing was kinetically arrested leading to a "fine-stranded" network that was similar for all "quench" depths for cooling rates slow enough to allow equilibrium hybridization. However, "quenches" with very high cooling rates led to a much coarser network.

The formation of low-density arrested structures in colloidal systems has been highly debated in the last years [19]. Several routes for gel formation have been thoroughly discussed, with particular emphasis on phase separation mediated gelation [20–23] and equilibrium gelation [24]. In the first case, the driving force for phase separation is central in producing dense regions, despite the small average sample concentration, in which dynamic arrests take place [25]. When this is the case, the frozen structure of the sample retains, encoded in its structure, information of the originating phase separation process. Vice versa in equilibrium gelation, expected to take place in low-valence systems, phase separation is not encountered on cooling and the progressively longer lifetime of the interparticle interaction is responsible of the slowing down of the dynamics and the eventual kinetic arrest. Even in the equilibrium gelation scenario deep quenches can induce diffusion limited aggregation, which can influence the structural evolution of the system [26, 27]. It is thus crucial, in order to identify the correct gelation scenario, to measure or calculate the equilibrium phase diagram of the investigated system. In the present paper we report the numerical study of a binary mixture of hard rods and hard spheres respectively reflecting the size and aspect ratio of the fd-virions and the size of the gold-NPs. As in the experiments [18], in the simulations only rods and spheres are assumed to attract via a short-range potential. We numerically explore the equilibrium phase diagram of the model, performing Monte Carlo simulations to probe its stability with respect to fluctuations of density in different phase points. We build the low-density branch of the system's binodal line as the boundary of the unstable two-phases region, confirming that in the experimental conditions the system undergoes a phase separation which —depending on the quench depth— can occur either via nucleation and growth or via spinodal decomposition. In particular, spinodal decomposition is shown to lead to the formation of percolating structures even at low densities. This confirms that DNA-coated rods and spheres form gels as a result on an interrupted phase separation, in analogy to spherical colloidal particles in the presence of polymer depletants [20–23].

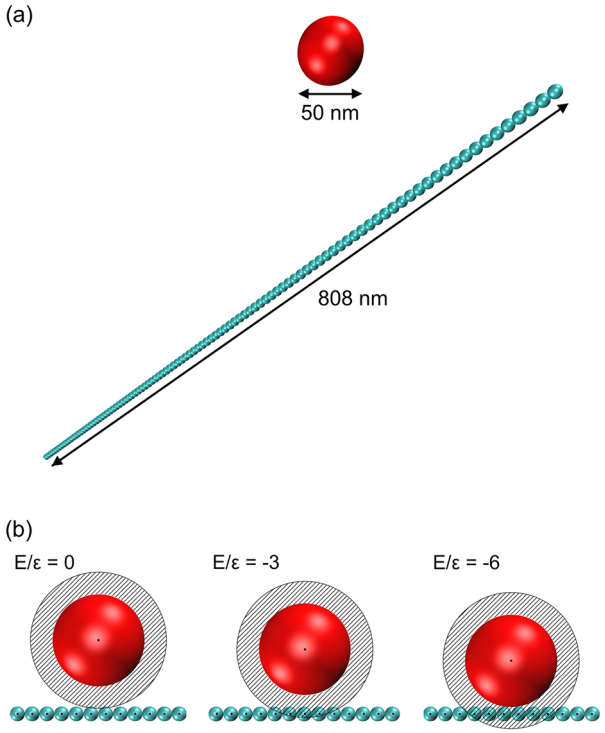

Fig. 1. (a) Representation of the particles. A hard rod is modelled as an ordered line of $N_b = 101$ spherical beads of diameter $\sigma_b = 0.16$ on a length scale fixed by the hard spheres' diameter $\sigma_G = 1$. (b) Representation of the attractive interaction in the model. From the left to the right the interaction energy E/ϵ between a hard sphere and a hard rod varies upon varying their relative distance. The maximum number of rod's beads interacting with the sphere via a square-well potential is six.

2 The model

We modelled the experimental system [18] as a binary mixture of hard spheres and hard rods. Specifically, gold nanoparticles were modelled as hard spheres of diameter $\sigma_G = 50$ nm and fd-viruses were modelled as hard rods of diameter $\sigma_b = 8$ nm and length $L_V = 0.808\,\mu$m, with an aspect ratio of 101, thus neglecting viruses' semi-flexibility. Notice that the persistence length of fd-viruses is $2.8 \pm 0.7\,\mu$m [28] and hence comparable to the viruses' length. Different approaches have been previously proposed and used in literature to model hard rods —*e.g.* the hard-cylinders model [29, 30] or the hard-spherocylinders model [31–33]. In order to mimic the granularity of the experimental DNA-driven interaction between virions and gold-NPs we decided to adopt a bead model for hard rods, namely modelling each hard rod as a rigid ordered line of $N_b = 101$ spherical beads of diameter σ_b (thus reflecting the chosen aspect ratio), as shown in fig. 1(a). We assumed hard sphere excluded volume interactions between gold-NPs, between beads composing two fd-viruses (providing a hard-core repulsion between each pair of hard rods) and between beads composing a virus and gold-NPs (providing an hard-core repulsion between each hard rod and each hard sphere). We assumed a short-range square-well (SW)

interaction of width $\Delta = 8\,\mathrm{nm}$ and depth ϵ (fixing our unit of energy) between each bead composing a virus and each gold nanoparticle, providing a short-range attraction depending on the relative distance between each hard rod and each hard sphere. Figures 1(a) and (b), respectively, provide a visual representation of the particles in the system and of the gold-virus interaction potential. Note that the full binding free energy $\beta\Delta G$ of the sequence α-α' used in the experiments was ~ 16.35 at room temperature. However, this value significantly changes with T (due to the large entropic contribution to DNA hybridisation), determining a sharp melting region of width roughly $10\,^{\circ}\mathrm{C}$.

Formally, the gold-gold (GG), the bead-bead (bb) and the gold-bead (Gb), pair potentials are

$$\Phi_{\mathrm{GG}}(r) = \begin{cases} \infty, & r < \sigma_{\mathrm{G}}, \\ 0, & r \geq \sigma_{\mathrm{G}}, \end{cases} \tag{1}$$

$$\Phi_{\mathrm{bb}}(r) = \begin{cases} \infty, & r < \sigma_{\mathrm{b}}, \\ 0, & r \geq \sigma_{\mathrm{b}}, \end{cases} \tag{2}$$

$$\Phi_{\mathrm{Gb}}(r) = \begin{cases} \infty, & r < \dfrac{(\sigma_{\mathrm{b}} + \sigma_{\mathrm{G}})}{2}, \\ -\epsilon, & \dfrac{(\sigma_{\mathrm{b}} + \sigma_{\mathrm{G}})}{2} \leq r < \dfrac{(\sigma_{\mathrm{b}} + \sigma_{\mathrm{G}})}{2} + \Delta, \\ 0, & r \geq \dfrac{(\sigma_{\mathrm{b}} + \sigma_{\mathrm{G}})}{2} + \Delta, \end{cases} \tag{3}$$

where r is the centre-to-centre distance respectively between a couple of gold-NPs, a couple of beads, and a bead and a gold nanoparticle. Notice that with the present choice of parameters, the lowest gold-virus interaction energy corresponds to -6ϵ (see fig. 1(b)), *i.e.* six adjacent rod beads can enter simultaneously in the bonding volume of the square-well.

We notice that in the experiments the observation of the cluster aggregates was performed on the gravity-deposited clusters on the bottom of the sample. We did not add gravitational fields in our calculations, as our aim was the evaluation of the equilibrium phase diagram and the identification of the gelation mechanism.

3 Numerical methods

We investigated the model with different Monte Carlo (MC) techniques.

3.1 Monte Carlo in the canonical ensemble

We performed simulations in the canonical ensemble, namely at fixed number of fd-viruses N_{V}, number of gold nanoparticles N_{G}, volume V and temperature T, with periodic boundary conditions, in a wide region of T and total volume fractions

$$\phi = \frac{3N_{\mathrm{V}}\pi\sigma_{\mathrm{b}}^2 L_{\mathrm{V}} + 2N_{\mathrm{G}}\pi\sigma_{\mathrm{G}}^3}{12V}\,.$$

We mostly kept the composition ratio $X \equiv N_{\mathrm{G}}/N_{\mathrm{V}}$ at the value $X = 5$ (one of the values explored in the experimental study). At each MC step we randomly chose one of the two species, and then one of the particles of the chosen species. We then performed a random displacement of the chosen particle. In case of a sphere, we just applied a random translation to its center with a maximum amplitude of $\pm 0.5\sigma_{\mathrm{G}}$. Instead for a rod we applied both a random displacement to its centre of mass —with a maximum amplitude of $\pm 0.5\sigma_{\mathrm{b}}$— and a random rotation to its direction —implementing the algorithm described in pag. 48 of ref. [34]. The algorithm requires a parameter γ controlling the maximum rotational angle that we set to $\gamma = 0.02$. The proposed displacement of the chosen particle was then accepted or rejected according to the standard Metropolis acceptance rule (see p. 30 of ref. [34]). Namely, if the proposed move led to the overlap of the displaced particle with any other particle in the system the move was automatically rejected. Otherwise, it was accepted with probability

$$\min\left(1, e^{-\beta\Delta U}\right),$$

where ΔU is the variation of energy eventually caused by the proposed move. Algorithms to check the overlap between any couple of particles were therefore necessary in order to test move acceptances. We designed an efficient algorithm to test the overlap between two bead-rods —based on the determination of the points of minimum distance between two line segments— that reduces the rod-rod overlap test to at most 5^2 sphere-sphere overlap tests between couple of beads. The efficient evaluation of the overlaps and the calculation of the binding energy between a hard rod and a hard sphere —based on the determination of the minimum distance between a line segment and a point— is afterwards simple to design.

We also implemented cluster moves. Clusters are defined as aggregates of bonded rods and spheres, where a bond between a sphere and a rod exists if their pair interaction is negative. During the MC simulation, every (on average) 50 MC steps we randomly picked a cluster and attempted to randomly translate it by at most $\pm 2.5\sigma_{\mathrm{G}}$ and rotate it (around the cluster's centre of mass) via a suitable random rotation matrix. If the chosen cluster was percolating —and thus infinitely extended given the periodic boundary conditions— the cluster move was rejected. To satisfy detailed balance without having to implement cluster-breaking moves, we accepted the cluster displacement if and only if it did not lead to overlaps or variations of the bonds in the system. We note that MC simulations produce a Brownian-like dynamic evolution —and hence the number of MC steps could be associated with a time evolution— only under specific conditions [35–38]. Similarly, cluster moves could be selected and adapted to mimic a Brownian —or even a hydrodynamic— evolution, coupling the translational and rotational displacement with the mass —or hydrodynamic radius— of the clusters [39, 40]. Since our study was not aimed at precisely characterizing the structure of the arrested phase, we did not try to implement these more sophisticated MC algorithms.

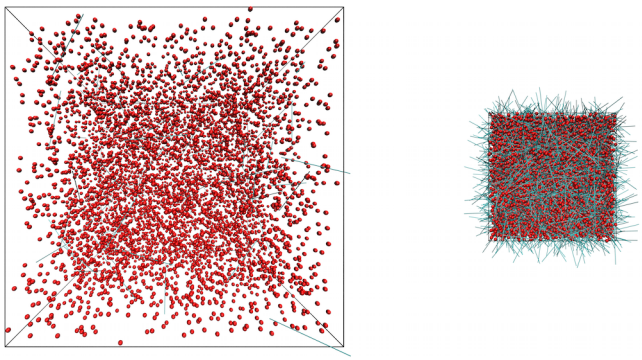

Fig. 2. Snapshot of a simulation in the Gibbs ensemble at $k_{\mathrm{B}}T/\epsilon = 1.6$, $\phi = 3.0\%$ and $X = 5$ of the parent phase.

3.2 Gibbs ensemble

To support the evidence of a phase separation and to provide estimates of the coexisting compositions along the experimental dilution line, we performed Gibbs ensemble simulations at different total packing fractions ϕ for the same temperature T. As in the original formulation [34, 41, 42], we studied two simulation boxes (I and II) in parallel, containing the two different phases of the system, which were characterized, respectively, by packing fractions ϕ_I and ϕ_{II} and compositions X_I and X_{II} (see fig. 2). At each MC step we randomly picked —with relative probabilities chosen in order to enhance equilibration— one of the following move proposals:

- Standard MC displacement move: a box and a species were randomly chosen, and the displacement of a random particle of the chosen species in the chosen box was proposed.
- Volume exchange moves: a complementary variation of the boxes' volumes $V_I \to V_I + \Delta V$ and $V_{II} \to V_{II} - \Delta V$ was proposed. ΔV was randomly picked with uniform probability in the interval $[-\delta V; \delta V]$, with $\delta V = 50^3\,\mathrm{nm}^3$.
- Particle exchange moves: a species and a box were randomly chosen and a random particle of the chosen species in the chosen box was proposed to be removed. This removal was proposed along with the insertion of the particle in a random state in the other box.

Each of this proposed moves was then eventually accepted according to specific acceptance rules designed by Panagiotopoulos [41, 42] in order to achieve phase equilibrium between the two boxes. The composition X, the number of particles N, the volume V and the temperature T of the total system —the so-called parent phase— were conserved throughout the simulation.

We performed Gibbs ensemble simulations with total packing fraction ϕ and composition X lying inside the unstable two-phase region. After reaching thermalization the coexisting phases (ϕ_I, X_I) and (ϕ_{II}, X_{II}) were determined. By varying the total ϕ and X it was possible to re-build the coexistence curves of the system in the ϕ-X plane for a given T.

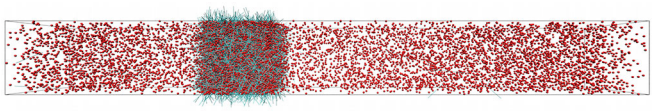

Fig. 3. Snapshot of a direct coexistence simulation at $k_{\mathrm{B}}T/\epsilon = 1.6$, $\phi = 3.0\%$ and $X = 5$.

3.3 Direct coexistence

Direct coexistence simulations, initially introduced by Ladd and Woodcock [43, 44] to study the triple point of Lennard-Jones models, allow for the determination of phase equilibria avoiding free energy calculations.

The method consists in performing a standard MC simulation in the canonical ensemble in the presence of two interfaces between two different phases (see fig. 3). During the simulation the total X, N, V —the parent phase— and T were thus conserved. Once thermalization was reached the bulk properties of the two coexisting phases (ϕ_I, X_I) and (ϕ_{II}, X_{II}) were measured.

4 Results and discussion

We focused on the fixed composition $X = N_{\mathrm{G}}/N_{\mathrm{V}} = 5$, experimentally studied in ref. [18], corresponding to a ratio of five hard spheres per hard rod. In the canonical ensemble, we investigated several ϕ —close to the one experimentally studied in ref. [18] $\phi = 0.1124\%$ (corresponding to a packing fraction $\phi_{\mathrm{G}} = 0.1\%$ of the only gold-NPs)— for several T. Starting from high T, where the system is properly described by a configuration of randomly disposed particles, we progressively lowered T and equilibrated the system. Below a cross-over T, equilibration became impossible within a simulation run, as the potential energy continued to drift during the entire run. The same cross-over T signalled a drop in the potential energy averaged over the last third of the simulation run. Such "instantaneous" drop of the energy upon a little variation of T is a hint of aggregation and first-order phase separation occurring in the system. Figure 4 shows the resulting low-density branch of the equilibrium phase diagram, in which open symbols mark phase points stable in the high-T and low-ϕ homogeneous phase, while filled symbols indicate phase-separating points. As shown in the inset, the line separating open and closed points —providing a proxy for the system's binodal line— were well approximated by $k_{\mathrm{B}}T/\epsilon = A\ln(\phi) + B$, using fitting parameters $A = 0.21$, $B = 1.77$.

The evolution of the potential energy during the simulation (see fig. 5) allowed us to distinguish between two possible mechanisms for phase separation. On the one hand, if the system was quenched below but near the binodal line —thus for shallow quenches into the two-phase region— the system underwent a phase separation consistent with a nucleation event: after remaining in the metastable fluid phase for a time t_w (t_w becomes longer when nearer to the binodal line), the system nucleates and grows mostly a single big cluster of the dense phase. On

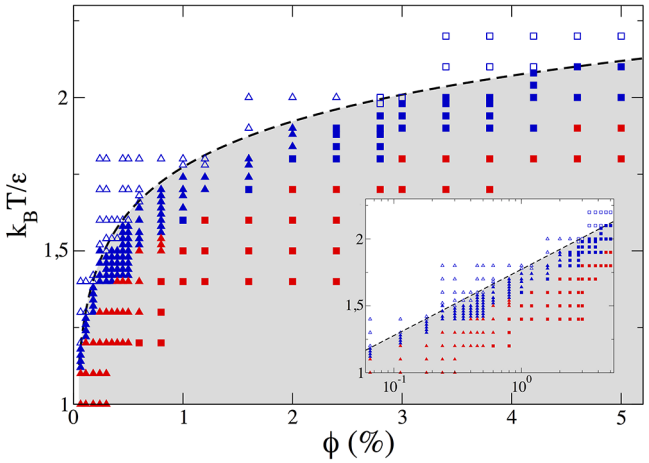

Fig. 4. Equilibrium phase diagram along the dilution line at composition $X = 5$. Open symbols define the region in which the system is in a homogeneous, stable fluid phase, while filled symbols identify state points in the unstable or metastable region that is dominated by density fluctuations. Specifically, blue filled points correspond to state points in which the system nucleates and grows the equilibrium phases, while filled red points correspond to points in which the system undergoes spinodal decomposition (see fig. 6). The dashed black line is our proxy for the system's binodal line. It is a fit of the function $k_BT/\epsilon = A\ln(\phi) + B$, with fitting parameters $A = 0.21$, $B = 1.77$. The shaded area below the binodal line is the unstable two-phase region, were the system phase-separates after a quench from high T. In the inset, the phase diagram is reported in semi-log scale. Squares indicate percolating state points.

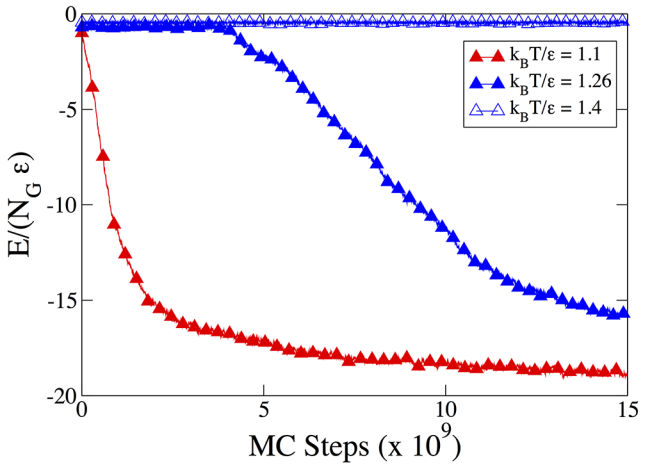

Fig. 5. Average potential energy (per sphere) as a function of the number of MC steps starting from a high-T configuration of packing fraction $\phi = 0.1124\%$ and $X = 5$ —a configuration of randomly distributed particles— quenched to different T (shown in the legend). The system at $k_BT/\epsilon = 1.4$ is stable in the high-T fluid phase, while phase separation occurs after quenches at $k_BT/\epsilon = 1.26$ and $k_BT/\epsilon = 1.1$, respectively leading to nucleation and spinodal decomposition (and to the final configurations shown in fig. 6).

the other hand, upon deeper quenches below the binodal line the system phase-separated via a spinodal decomposition mechanism, characterized by a slow and continuous decrease of the potential energy associated to the local growth of many small clusters immediately after the quench. The two different mechanisms are marked by full symbols with different colors in fig. 4. Snapshots of the phase-separated system, both via nucleation and phase separation, at the end of the simulation are shown in fig. 6 (top). Supporting videos of the system undergoing nucleation (SV1) and spinodal decomposition (SV2) are provided as Supplementary Material to this paper. The evolution of the spheres' structure factor [45] $S(q)$ is consistent with the previous classification: after a quench from the fluid phase —characterized by an essentially flat $S(q)$— into the two-phase region a low-q signal arises in the structure factor, strongly dependent on the phase separation mechanism. On the one hand, the evolution of $S(q)$ along the nucleation-and-growth route is characterized by a growing signal for $q \to 0$. On the other hand the fastest signal's growth in $S(q)$ takes place at a finite low-q value along spinodal decomposition. The $S(q)$ evolution, both during nucleation and during spinodal decomposition, is shown in fig. 6 (bottom). Interestingly, even if a clear growth of a peak in $S(q)$ at finite q was observed in experiments, the nucleation-and-growth regime was elusive. The reason for this is most likely the fact that nucleation is quickly followed by sedimentation, driven by the larger density of the aggregates. Hence clusters started to form and sediment while still small, depleting the top fluid surface and therefore stopping the growth phase. This could explain why even at low quenches the samples appeared to have undergone a spinodal decomposition process.

To estimate if the numerically generated phase-separated configurations —in particular the ones obtained in the spinodal region— could be associated with percolating configurations, at least in a kinetically arrested condition, we extended the previous simulations turning on cluster moves. These moves, by collectively displacing groups of bonded particles, led to diffusion and aggregation of clusters and favoured a further decrease of the potential energy until a completely arrested state was reached. Such arrested state was not necessarily an equilibrium state, but eventually a non-equilibrium kinetically arrested state, whose structure was therefore strongly influenced by the system's out-of-equilibrium dynamics. Therefore our simulations —not providing a reliable out-of-equilibrium Brownian or hydrodynamical dynamics (see sect. 3.1) and not taking into account gravity— could not capture the real structure of the resulting arrested state. Nevertheless, they showed that phase separation can lead to percolation in the system —which for instance can only be favoured by the action of gravity. Several of the final arrested configurations at the end of the cluster move simulations were indeed characterized by the presence of a percolating cluster, even at low packing fractions. These percolating states are marked as squares in fig. 4. In fig. 7 a snapshot of the final configuration of a simulation with and without cluster moves is shown. Therefore, when the system was deeply quenched into the two-phase unstable region, phase separation via spinodal

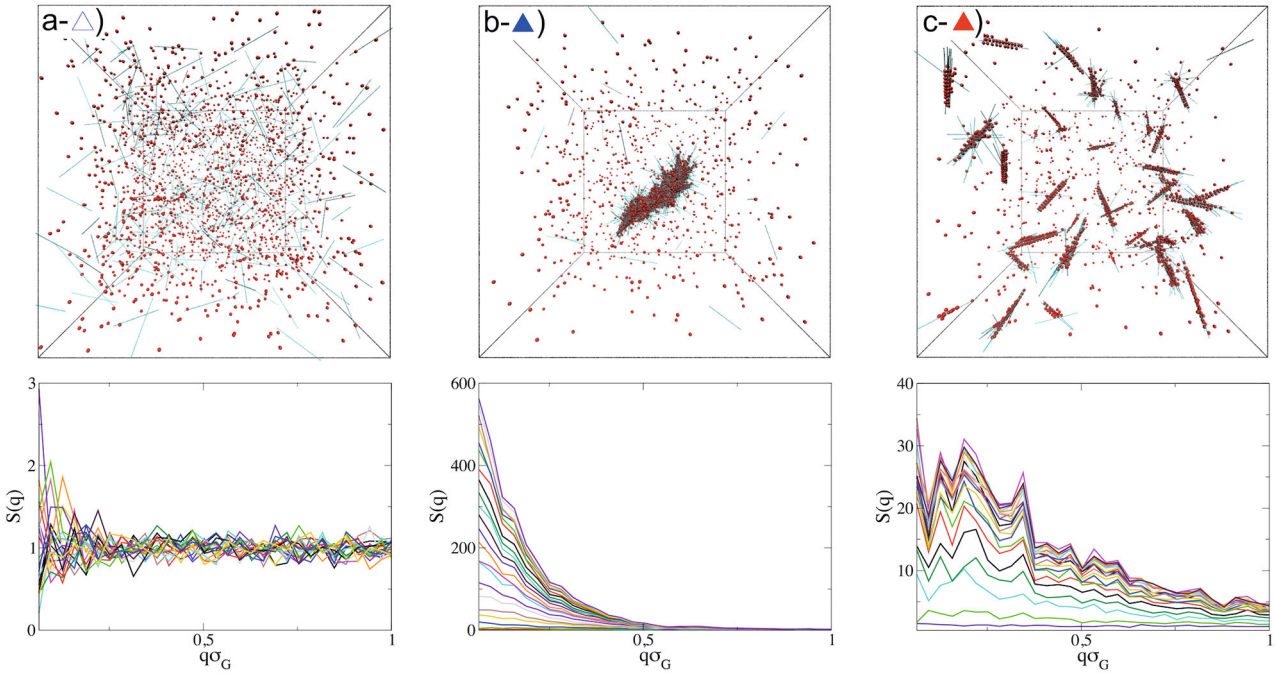

Fig. 6. Top panels: Snapshots of the system at $\phi = 0.1124\%$ (corresponding to the experimental ϕ) in the fluid phase (a: $k_{\mathrm{B}}T/\epsilon = 1.4$) and after a shallow quench leading to nucleation (b: $k_{\mathrm{B}}T/\epsilon = 1.26$) and a deep quench leading to spinodal decomposition (c: $k_{\mathrm{B}}T/\epsilon = 1.1$). The difference between the two separation mechanisms is evident: nucleation leads to the growth of a single cluster of the dense aggregated phase after a certain time spent in the metastable fluid phase, while spinodal decomposition leads to the aggregation of many small local clusters immediately after the quench. Bottom panels: Evolution in time of $S(q)$ in the fluid phase (a: $k_{\mathrm{B}}T/\epsilon = 1.4$) and during phase separation both via nucleation (b: after a quench at $k_{\mathrm{B}}T/\epsilon = 1.26$) and via spinodal decomposition (c: after a quench at $k_{\mathrm{B}}T/\epsilon = 1.1$).

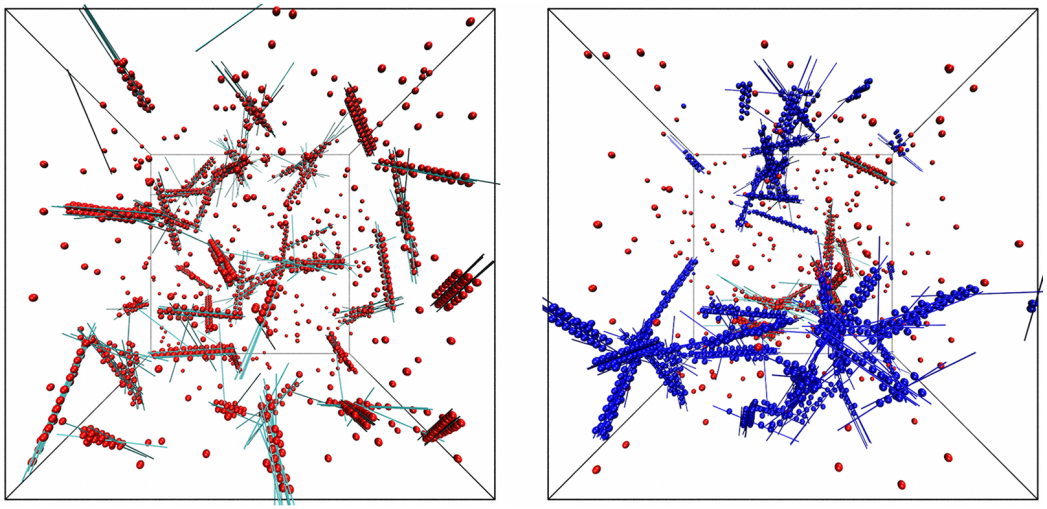

Fig. 7. Snapshots of the system of packing fraction $\phi = 0.45\%$ at temperature $k_{\mathrm{B}}T/\epsilon = 1.2$ in the final configuration of a simulation with (right) and without (left) cluster moves. Cluster moves allow for the diffusion and aggregation of clusters and may lead to the formation of a percolating network of clusters (coloured in deep blue) in the final configuration of the simulation, namely to percolation in the system.

decomposition led to the formation of many small clusters that showed no correlation at all in their orientations, although presenting some internal orientational order (see sect. 4.1). These small clusters —randomly displaced and oriented inside the simulation box— then progressively diffused and merged, eventually leading to a percolating arrested state even at low densities. This, along with the evidence of a spinodal decomposition occurring in the system in the experimental conditions, allowed us to label the experimental gelation of the system as a non-equilibrium gelation via arrested spinodal decomposition. We note on passing that in all of our standard Monte Carlo simulations the total excluded volume of the hard rods component never exceeds the value theoretically predicted by

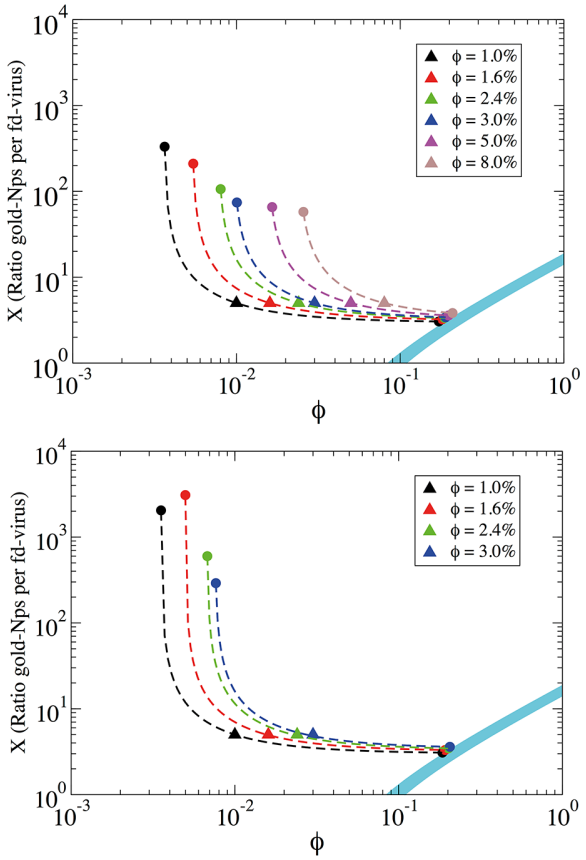

Fig. 8. Coexisting phases at temperature $k_BT/\epsilon = 1.6$ determined (a) in the NVT-Gibbs ensemble and (b) via direct coexistence. Triangles represent the ϕ and X of the uniform parent phases (the total ϕ and the total X of the full system). Filled circles of the same colour indicate the resulting coexisting phases. The dashed lines, connecting the coexisting phases and passing through the parent phase, indicate all total X and ϕ that would separate in the same coexisting phases. The cyan shaded area indicates points in which the packing fraction of the only hard rods is in the coexistence region of the isotropic-to-nematic phase transition of a pure rods' system evaluated according to Onsager's theory. Notice that one of the coexisting phases in which the system phase-separates approaches the isotropic-to-nematic phase transition for the hard rods, coherently with the tendency of the dense phase to order into nematic-like ordered structures discussed in sect. 4.1 and in the conclusions.

Onsager [1] for the isotropic-to-nematic phase transition of a pure rods' system. Specifically, the packing fraction of the total system (both hard rods and hard spheres) at which the excluded volume of the only hard rods is the theoretically predicted one at the isotropic-to-nematic phase transition varies with the composition of the system, as shown in fig. 8.

The phase diagram presented in fig. 4 provides an indication of the T-ϕ region where a homogeneous solution with $X = 5$ becomes thermodynamically unstable. Due to the binary nature of the system, such a line does not provide an indication of the coexisting equilibrium phases when the homogeneous state point is quenched inside the unstable region. To support the evidence of a phase separation and to estimate the coexisting densities in the X-ϕ plane at least for one T (namely $k_BT/\epsilon = 1.6$), we performed simulations in the NVT-Gibbs ensemble. The results for six different starting packing fractions, all at $X = 5$, are reported in fig. 8(a). In all cases we observed that the system phase-separates in a very low-density fluid phase mainly composed of spheres, whose composition strongly varied with ϕ of the parent phase, and a very-high-density phase whose composition did not change significantly upon variations of the parent phase, being typically about $X \sim 3$–4.

To further support these results, we performed direct coexistence simulations of four of the six parent phases studied via Gibbs ensemble simulations. The resulting estimates for the coexisting phases at temperature $k_BT/\epsilon = 1.6$ are reported in fig. 8(b). The results of direct coexistence simulations confirmed the tendency of the system to phase-separate in a low-density fluid phase mainly composed of spheres and a high-density phase of composition weakly depending on the parent phase. In particular, the ϕ of both the low- and high-density phases and the composition of the high-density phase compare well with the results of Gibbs ensemble simulations. We note that the values of the composition of the low-density phase differ between the two numerical methods, signalling a numerical difficulty in properly equilibrate the rods between the two phases. Still, the evidence of a phase separation is indisputable.

4.1 Low-temperature clusters structure

The final configurations of the simulations provided information on the structure of the aggregates. At low ϕ, clusters were formed by junction points, in which a large number of rods coalesce with different orientations and long straight arms are formed by several parallel rods decorated with gold-NPs. These arms (see fig. 9(a)) could act as nuclei of an incipient crystallization process, being formed by highly ordered structures that could be replicated in space, forming planar extended structures. Indeed, we find that each rod has at most ≈ 32 contacts with spheres, *i.e.* two full rows of spheres (up to 16 aligned spheres could geometrically bind to each rod). Also in the experiments hints of such local alignment were observed when the aggregated structures were analysed in term of a chord-analysis [18]. However, working at the limit of the optical resolution of the microscope, we were not able to identify these ordered structures on particle scales. We also note that most of the time we observe partially incomplete rows of spheres coordinated to the same rod, leaving some space for rattling. To quantify this observation, fig. 9(b) shows the radial distribution function of the spheres, characterized by a first main peak at values of $r \approx 60$ nm, 20% higher than the spheres' contact distance.

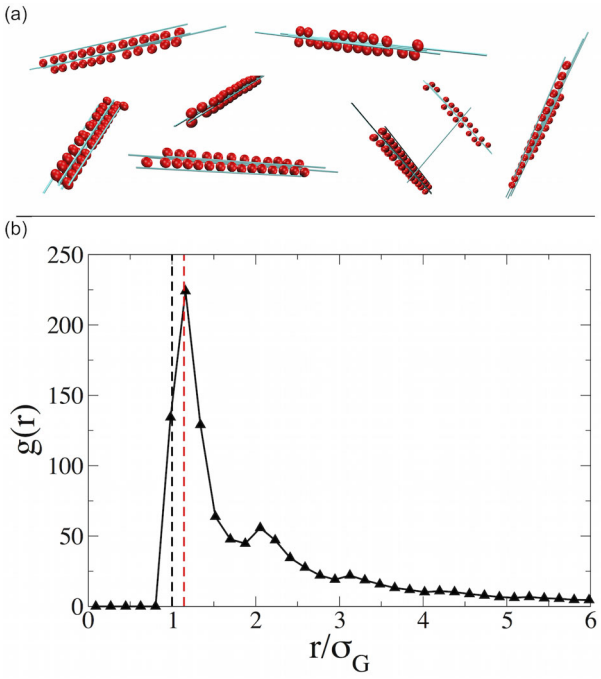

Fig. 9. (a) Representation of small clusters observed during spinodal decomposition in the system at $\phi = 0.1124\%$ after a quench from $k_BT/\epsilon = 1.4$ to $k_BT/\epsilon = 1.1$, below the binodal line. (b) Radial distribution function of spheres in the system at $\phi = 0.1124\%$ after spinodal decomposition at $k_BT/\epsilon = 1.1$. A first peak is present at $r \approx 60\,\text{nm}$, compatible with a typical spacing between the spheres bundled in the clusters.

5 Conclusions

The identification of the gelation mechanism active in a binary mixture of complementary DNA-functionalized fd-viruses and gold-NPs has motivated the present investigation. The reported Monte Carlo simulations suggest that indeed a thermodynamic instability initiates the phase separation process, producing regions in which rods interconnected via gold-NPs condensate. Gibbs-ensemble and direct coexistence simulations confirm the presence of a phase separation phenomenon in the X-ϕ windows explored by the experiments. These results allow us to classify the experimentally observed arrest mechanism as an interrupted phase separation, *i.e.* in the same category as colloidal gelation in the presence of depletants [20–23]. We observe both nucleation and spinodal decomposition phenomena, thereby extending our insight into the system beyond what is experimentally possible. As confirmed by Gibbs ensemble and direct coexistence simulations, both nucleation and spinodal decomposition lead to phase equilibrium between a low-density spheres-rich phase and a high-density phase of composition $X \sim 3$–4. While nucleation generates few isolated clusters of the dense phase in equilibrium with a less dense phase composed essentially of isolated gold particles, the spinodal decomposition path generates fluctuations of the density with a characteristic length scale (evidenced by a growing maximum at a finite wave vector in $S(q)$), leading to the formation of multiple clusters. The diffusion and aggregation of these clusters leads —even at small ϕ— to the formation of percolating networks in the system. Analysis of the configurations shows that the network is formed by branching points in which several orientationally disordered rods are linked together by spheres, providing a microscopic description of the non-resolved structures observed by fluorescence microscopy imaging carried on the system in ref. [18]. This analysis should however be taken with a pinch of salt, considering that the networks resulting from our simulations are generated with an un-physical out-of-equilibrium dynamics and in the absence of gravity. At low T, the packing of spheres around rods induces some local ordering. Even though the overall orientation of rods remains uncorrelated, this is the hint of a tendency of the system to orientationally order in the dense phase. An equilibrium high-density crystal or nematic phase of composition $X \sim 3$–4 coexisting at equilibrium with a low-density spheres-rich fluid phase, not observed because of the dynamical arrest of the system in a non-equilibrium arrested state, cannot be excluded.

We acknowledge support from ITN-Colldense. E. Eiser is grateful to Sapienza, Universita' di Roma for supporting her stay in Rome as visiting scientist.

Author contribution statement

All authors contributed equally to the paper.

References

1. L. Onsagher, Ann. N.Y. Acad. Sci. **51**, 627 (1949).
2. S. Fraden, G. Maret, D.L.D. Caspar, R.B. Meyer, Phys. Rev. Lett. **63**, 2068 (1989).
3. S. Fraden, G. Maret, D.L.D. Caspar, Phys. Rev. E **48**, 2816 (1993).
4. R. Oldenbourg, X. Wen, R.B. Meyer, D.L.D. Caspar, Phys. Rev. Lett. **61**, 1851 (1988).
5. Z. Dogic, S. Fraden, Curr. Opin. Colloid Interface Sci. **11**, 47 (2006).
6. Z. Dogic, K.R. Purdy, E. Grelet, M. Adams, S. Fraden, Phys. Rev. E **69**, 051702 (2004).
7. P.A. Buining, A.P. Philipse, H.N.W. Lekkerkerker, Langmuir **10**, 2106 (1994).
8. H. Maeda, Y. Maeda, Phys. Rev. Lett. **90**, 018303 (2003).
9. A. Kuijk, D. Byelov, A.V. Petukhov, A. van Blaaderen, A. Imhof, Faraday Discuss. **159**, 181 (2012).
10. Z.X. Zhang, J.S. van Duijneveldt, J. Chem. Phys. **124**, 154910 (2006).
11. J. Peng, A. Kroes-Nijboer, P. Venema, E. van del Linden, Soft Matter **12**, 3514 (2016).
12. M. Adams, Z. Dogic, S.L. Keller, S. Fraden, Nature **393**, 349 (1998).
13. N. Yasarawan, J.S. van Duijneveldt, Soft Matter **6**, 353 (2010).
14. C.A. Mirkin, R.L. Letsinger, R.C. Mucic, J.J. Storhoff, Nature **382**, 607 (1996).

15. A.P. Alivisatos, K.P. Johnsson, X. Peng, T.E. Wilson, C.J. Loweth, M.P.J. Bruchez, P.G. Schultz, Nature **382**, 609 (1996).
16. N. Geerts, E. Eiser, Soft Matter **6**, 4647 (2010).
17. R.R. Unwin, R.A. Cabanas, T. Yanagishima, T.R. Blower, H. Takahashi, G.P.C. Salmond, J.M. Edwardson, S. Fraden, E. Eiser, Phys. Chem. Chem. Phys. **17**, 8194 (2015).
18. Z. Ruff, S.H. Nathan, R.R. Unwin, M. Zupkauskas, D. Joshi, G.P.C. Salmond, C.P. Grey, E. Eiser, Faraday Discuss. **186**, 473 (2016).
19. E. Zaccarelli, J. Phys.: Condens. Matter **19**, 323101 (2007).
20. P.J. Lu, E. Zaccarelli, F. Ciulla, A.B. Schofield, F. Sciortino, D.A. Weitz, Nature **453**, 499 (2008).
21. E.H.A. de Hoog, W.K. Kegel, A. van Blaaderen, H.N.W. Lekkerkerker, Phys. Rev. E **64**, 021407 (2001).
22. F. Cardinaux, T. Gibaud, A. Stradner, P. Schurtenberger, Phys. Rev. Lett. **99**, 118301 (2007).
23. S. Buzzaccaro, R. Rusconi, R. Piazza, Phys. Rev. Lett. **99**, 098301 (2007).
24. E. Bianchi, J. Largo, P. Tartaglia, E. Zaccarelli, F. Sciortino, Phys. Rev. Lett. **97**, 168301 (2006).
25. F. Sciortino, R. Bansil, H.E. Stanley, P. Alstrom, Phys. Rev. E **47**, 4615 (1993).
26. F. Sciortino, P. Tartaglia, Phys. Rev. Lett. **74**, 282 (1995).
27. M. Carpineti, M. Giglio, Phys. Rev. Lett. **68**, 3327 (1992).
28. E. Barry, D. Beller, Z. Dogic, Soft Matter **5**, 2563 (2009).
29. M.C. Duro, J.A. Martn-Pereda, L.M. Ses, Phys. Rev. A **37**, 284 (1988).
30. R. Blaak, D. Frenkel, B.M. Mulder, J. Chem. Phys. **110**, 11652 (1999).
31. D. Frenkel, H.N.W. Lekkerkerker, A. Stroobants, Nature **332**, 822 (1988).
32. J.A.C. Veerman, D. Frenkel, Phys. Rev. A **41**, 3237 (1990).
33. M. Dijkstra, R. van Roij, R. Evans, Phys. Rev. E **63**, 051703 (2001).
34. D. Frenkel, B. Smit, *Understanding Molecular Simulation: From Algorithms to Applications*, *Computational Science Series*, Vol. **1** (Academic Press, 2002).
35. E. Sanz, D. Marenduzzo, J. Chem. Phys. **132**, 194102 (2010).
36. F. Romano, C.D. Michele, D. Marenduzzo, E. Sanz, J. Chem. Phys. **135**, 124106 (2011).
37. A. Patti, A. Cuetos, Phys. Rev. E **86**, 011403 (2012).
38. A. Cuetos, A. Patti, Phys. Rev. E **92**, 022302 (2015).
39. M. Rottereau, J.C. Gimel, T. Nicolai, D. Durand, Eur. Phys. J. E **15**, 133 (2004).
40. S. Babu, J.C. Gimel, T. Nicolai, J. Chem. Phys. **125**, 184512 (2006).
41. A.Z. Panagiotopoulos, Mol. Phys. **61**, 813 (1987).
42. A.Z. Panagiotopoulos, N. Quirke, M. Stapleton, D.J. Tildesley, Mol. Phys. **63**, 527 (1988).
43. A.J.C. Ladd, L.V. Woodcock, Chem. Phys. Lett. **51**, 155 (1977).
44. A.J.C. Ladd, L.V. Woodcock, Mol. Phys. **36**, 611 (1978).
45. J.-P. Hansen, I.R. McDonald, *Theory of Simple Liquids*, 3rd edition (Academic Press, 2006).